



PII S0016-7037(99)00046-0

Origin of compact type A refractory inclusions from CV3 carbonaceous chondrites

S. B. SIMON,¹ A. M. DAVIS,^{1,2} and L. GROSSMAN^{1,2}¹Department of the Geophysical Sciences²Enrico Fermi Institute, The University of Chicago, Chicago, Illinois, USA

(Received June 10, 1998; accepted in final form October 13, 1998)

Abstract—Compact type A (CTA) inclusions are one of the major types of coarse-grained refractory inclusions found in carbonaceous chondrites. They have not been studied in a systematic fashion, leading to some uncertainties and unproven assumptions about their origin. To address this situation, we studied a total of eight CTAs from Allende, Efremovka and Axtell by scanning electron-microscopic and electron and ion-microprobe techniques. These inclusions are very melilite-rich, ranging from ~60 vol% to nearly monomineralic. Also present are Mg–Al spinel (5–20%), perovskite (trace–~3%) and, in some samples, Ti-rich (~17 wt% TiO₂) fassaite (trace–~20%), and rhönite (≤1%). Melilite compositions are mostly between Åk₁₅ and Åk₄₀. Chondrite-normalized REE abundance patterns for melilite (flat at ~10 × CI with positive Eu anomalies) and fassaite (slight HREE enrichment relative to LREE and negative Eu anomalies) are like those for their counterparts in once-molten type B inclusions. The patterns for rhönite have positive slopes from La through Lu and abundances <10 × CI for La and 35–60 × CI for Lu. Features of CTAs that suggest that they were once molten include: rounded inclusion shapes; positively correlated Sc and V abundances in fassaite; radially oriented melilite laths at inclusion rims; and the distribution of trace elements among the phases. Fractional crystallization models show that, with one exception, the REE contents of perovskite and fassaite arose by crystallization of these phases from late, residual liquids that would have resulted from prior crystallization of the observed proportions of melilite and spinel from liquids having the bulk compositions of the inclusions. One Allende CTA (TS32), however, has several features (irregular shape, reversely zoned melilite, fassaite REE contents) that are not readily explained by crystallization from a melt. This inclusion may have undergone little melting and may be dominated by relict grains. Copyright © 1999 Elsevier Science Ltd

1. INTRODUCTION

Type A inclusions are one of the two main types of coarse-grained, refractory inclusions recognized by Grossman (1975) in a study of inclusions from the Allende CV3 carbonaceous chondrite. Type A Ca-, Al-rich inclusions (CAIs) were defined by Grossman (1975) as those with 80–85% melilite and 15–20% spinel, while inclusions with 5–20% melilite and 35–60% pyroxene were termed type Bs. It is now accepted that type B inclusions were once molten (e.g., MacPherson and Grossman, 1981; MacPherson et al., 1984; Stolper and Paque, 1986). Type A inclusions were subdivided into irregularly shaped ones and rounded ones by MacPherson and Grossman (1979). These two subtypes were later termed “fluffy” and “compact”, respectively, by Grossman (1980). Fluffy type As (FTAs) were studied by MacPherson and Grossman (1984), who concluded that they most likely formed by gas–solid condensation. Until now, there has been no analogous systematic study of compact type As (CTAs). Although various features of many CTAs have been studied and many workers assume that they crystallized from liquids, this has not been demonstrated and their origin is somewhat controversial. Fuchs (1978) studied one CTA and cited petrographic and mineral-chemical evidence that it crystallized from a liquid but could not present a thermal history that would account for all the observations.

Wark and Lovering (1982) concluded that CTAs were condensates, whereas Teshima and Wasserburg (1985) studied three CTAs and concluded that they had crystallized from liquids after being completely molten and then were metamorphosed to different degrees, causing “little to complete recrystallization.” Fahey et al. (1987) studied one CTA in detail but could not conclude whether or not it was ever molten. Podosek et al. (1991) studied one CTA and found no features, except for the rounded shape of the inclusion, consistent with formation by melt solidification. Simon et al. (1998) also studied one CTA in detail and proposed a complex thermal history involving rapid crystal growth from a melt followed by slow cooling to explain the unusual features of the inclusion they studied. Greshake et al. (1998) studied three CTAs and concluded that they had experienced a partially molten state followed by recrystallization. In addition, Paque and Stolper (1984) and Beckett (1986) experimentally investigated the equilibrium crystallization sequence for several type A-like bulk compositions, but, in general, the crystallization histories of compact type A inclusions are not well understood. We have undertaken a study of a suite of CTAs from Allende and Axtell, members of the oxidized subgroup of CV3 chondrites (McSween, 1977), and Efremovka, a member of the reduced subgroup. The purposes of this study are to document, for the first time, in one investigation, the petrographic, mineral-chemical, and trace-element features of a representative suite of CTAs, and to use these data and observations to determine how these objects formed. Preliminary results of this investigation were given by Davis et al. (1990) and Simon et al. (1995).

Address reprint requests to Dr. S. B. Simon, Dept. of the Geophysical Sciences, The University of Chicago, 5734 S. Ellis Avenue, Chicago, IL 60637; Fax: (773) 702-9505.

2. ANALYTICAL METHODS

Polished thin sections of each sample (with the exception of A37, for which only a polished thick section was available) were studied petrographically (optically and with a scanning electron microscope, or SEM), and analyzed by electron and ion microprobes. Backscattered electron images and digital X-ray maps were obtained with a JEOL JSM-5800 LV scanning electron microscope equipped with an Oxford/Link ISIS-300 energy-dispersive X-ray microanalysis system (EDS). Quantitative wavelength-dispersive analyses were obtained with a Cameca SX-50 electron probe operated at 15 kV. Data were reduced via the modified ZAF correction procedure PAP (Pouchou and Pichoir, 1984). Trace-element analyses were obtained with the University of Chicago AEI IM-20 ion microprobe. The analytical techniques used are similar to those described in Simon et al. (1991) and MacPherson and Davis (1993, 1994).

3. RESULTS

3.1. Samples

CTAs exhibit a range of textures, from those dominated by equigranular melilite grains that meet at 120° triple junctions to others that are dominated by coarse laths like those found in type B inclusions. We studied five CTAs from Allende (TS12, TS19, TS32, TS68, and A37), one from Efremovka (Ef3), and two from Axtell (AX4, AX30) that cover this range. Of these, two inclusions, TS68 and Ef3, have $\sim 15\%$ fassaite; the remainder are very fassaite-poor and consist of melilite + spinel + alteration products, with $\sim 1\%$ perovskite \pm fassaite. A trace amount of rhönite is present in A37. The sample from Efremovka is very low in alteration products, which is typical of inclusions from the reduced subgroup of CV3 chondrites. Each sample is briefly described in what follows.

3.2. Petrography

TS12 is crescent-shaped, 8 mm long, and ~ 1.5 mm across, and dominated by coarse melilite grains oriented at high angles to the inclusion rim. It has a $70\text{-}\mu\text{m}$ -thick sequence of three mineralogically distinct layers of the type described by Wark and Lovering (1977), hereinafter called Wark–Lovering rims, present only on the long, outer, curved edge of the inclusion. The three layers, from innermost to outermost, are aluminous diopside, perovskite + spinel and hibonite + spinel. Melilite crystals range from small ($200 \times 100 \mu\text{m}$) blocky grains to laths 1.5 mm long and 0.7 mm wide. Some shock lamellae (peg structure) are observed in transmitted light, as shown by Grossman (1975), but most grains have uniform birefringence and are not strongly zoned. Some melilite–melilite contacts are straight and others are sutured. Most melilite grains poikilitically enclose spinel grains, most of which are subhedral or euhedral and $20\text{--}100 \mu\text{m}$ across. Some grains are rounded. Perovskite is present mostly as small, rounded grains less than $20 \mu\text{m}$ across, but sizes range up to $\sim 100 \mu\text{m}$. In general, in this inclusion the grain size and abundance of spinel increase with increasing distance from the Wark–Lovering rim, varying from virtually absent within $\sim 300 \mu\text{m}$ of the rim to the edge furthest from the Wark–Lovering rim, where $100\text{-}\mu\text{m}$ -sized spinel grains are in contact with each other or have only perovskite between them.

TS19 is an irregularly shaped, fragmented inclusion. A backscattered electron image (BEI) of a representative area is shown in Figure 1a. (See also Fahey et al. [1987] and Podosek et al.

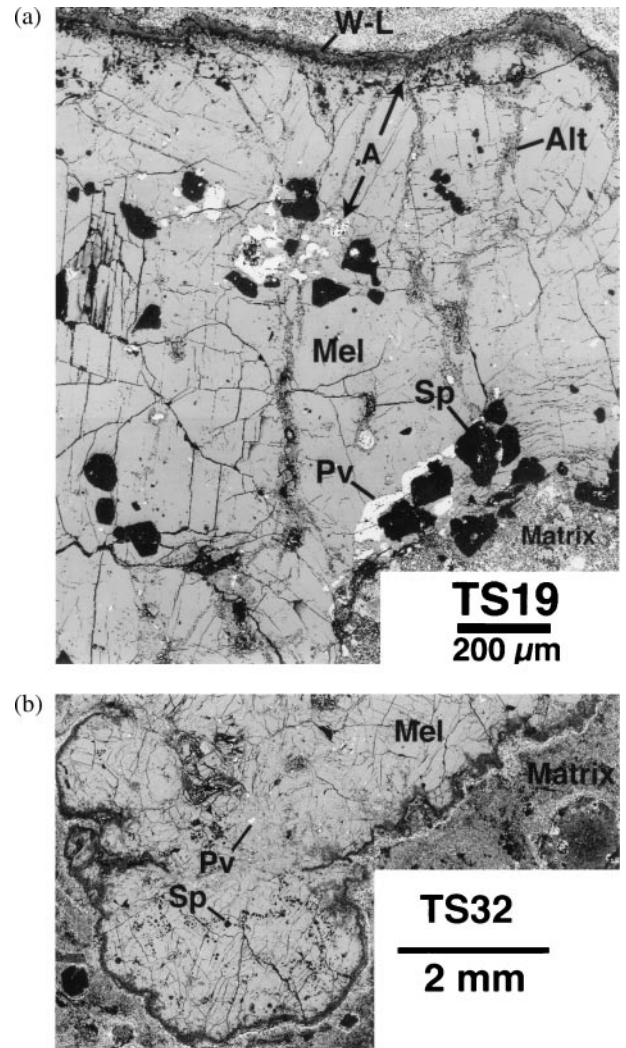


Fig. 1. (a) Backscattered electron image (BEI) of a representative portion of TS19. Note the coarse spinel (Sp) and perovskite (Pv) and high abundance of melilite (Mel). Veins of alteration products (Alt) and the Wark–Lovering rim (W–L) are also visible. Grain labeled “A” is an example of a crystal oriented at a high angle to the inclusion rim. (b) BEI of a portion of TS32. Note the irregular shape and numerous embayments in the rim, in contrast to the smooth rim of TS19.

[1991] for general views of CTAs.) A Wark–Lovering rim is present along the original edges of the inclusion. The inclusion is dominated by coarse, subhedral melilite grains, typically $\sim 700 \mu\text{m}$ across and displaying cleavage traces, undulose extinction, and peg structure. Smaller (up to $\sim 400 \mu\text{m}$), somewhat stubby crystals occur just inside the Wark–Lovering (W–L) rim, at high angles to it. These can be seen in the upper part of Figure 1a, such as the grain labeled “A,” partially outlined by alteration products. Spinel grains are round to subhedral, $10\text{--}100 \mu\text{m}$ across, and occur in chains, clumps, and as isolated grains. Also present are numerous grains of fine spinel, $< \sim 1 \mu\text{m}$ across. Perovskite occurs as anhedral, rounded, blebby grains ranging in size from several microns to $\sim 100 \mu\text{m}$ across. They occur enclosed in melilite and spinel, and along melilite–melilite contacts.

TS32 is an irregularly shaped, lightly altered inclusion with

melilite laths up to ~ 1.3 mm long and blocky melilite grains up to ~ 1 mm across. A BEI of part of the inclusion is shown in Figure 1b. Many grains exhibit peg structure and undulose extinction, but otherwise optical zoning is not apparent in the melilite. Most melilite grains are spinel-free, but there are some spinel-rich areas in which melilite encloses euhedral spinel grains that are up to ~ 50 μm across. Rare, anhedral fassaite grains, up to ~ 150 μm long, occur wedged between the much coarser melilite. Fassaite is very difficult to see in BEIs of CTAs, because, in these samples, it has high Ti oxide contents that give it an electron albedo very close to that of melilite. Perovskite occurs as rounded grains, up to 20 μm across, enclosed in melilite, as small grains adjacent to spinel, and in symplectic wormy intergrowths with spinel and fassaite, one of which is shown in Figure 2a. Symplectites in CTAs have been described previously (Haggerty, 1976; El Goresy et al., 1977; Fuchs, 1978) and were first thought to result from the decomposition of rhönite (Haggerty, 1976), a rare Ti-rich silicate (see later). Experiments by Beckett (1986) showed, however, that equilibration temperatures for perovskite–spinel–fassaite symplectites are within the range of those determined for rhönite–fassaite equilibration, and led him to conclude that symplectites formed from late-stage, Ti-rich liquids, as had been suggested by El Goresy et al. (1977) and Fuchs (1978).

A Wark–Lovering rim completely encloses TS68, which has a smooth shape. Stubby melilite crystals up to 400 μm long occur adjacent to the inclusion rim and are oriented at high angles to it, as shown in Figure 2b. Inside of this zone, coarser melilite crystals, up to ~ 700 μm across occur, also oriented at high angles to the rim. As in the CTAs just described, the melilite occurs in an interlocking texture and most grains do not exhibit strong optical zonation. Spinel occurs as euhedral grains, mostly 20–100 μm across, very unevenly distributed throughout the inclusion. Spinel is sparse to absent in the outer 700 μm of the inclusion and about one third of the inclusion is virtually spinel-free, whereas some areas are quite spinel-rich, with clumps, chains, and dense concentrations of spinel grains. Unlike most CTAs, TS68 contains coarse fassaite, occurring as round, anhedral grains up to ~ 1 mm across in spinel-rich areas of the inclusion, and poikilitically enclosing spinel. Smaller anhedral fassaite grains, 30–100 μm across, occur enclosed in melilite and between melilite grains. Perovskite occurs as rare, anhedral, isolated grains that are typically 20–50 μm across. CAIs commonly contain opaque mineral assemblages, termed Fremdlinge by El Goresy et al. (1978), that consist of FeNi-metal, Pt-metal alloys, V-rich magnetite, sulfides, and phosphates in various proportions. Fremdlinge in TS68 are abundant and S-rich but contain all these phases, and commonly occur enclosed in V-rich fassaite. Fremdlinge from TS68 were analyzed via instrumental neutron activation analysis (INAA) by Sylvester et al. (1992).

Only a polished thick section of A37 was available to us for study, but this sample is important because its trace-element contents have been determined (Bischoff et al., 1987) and because it contains rhönite, a rare, Ti-rich silicate, which was first found in meteorites (in a CTA) by Fuchs (1971). The rim of the inclusion contains spinel, perovskite, and hibonite, and was discussed in some detail by Bischoff et al. (1987). Within the inclusion, spinel occurs as subhedral to euhedral crystals 20–70 μm across. It is sparsely distributed throughout the outer

~ 700 μm of the inclusion and much of the interior. There are, however, several regions, each up to ~ 1 mm across, that are quite rich in spinel. The inclusion contains fassaite grains that are typically ~ 100 μm across and occur between melilite grains. Unlike those in TS68, the fassaite grains in A37 are spinel-free. Rhönite grains, one of which is shown in Figure 2c, are anhedral, 20–100 μm across and appear to occur between melilite grains or between melilite and fassaite grains. Most rhönite crystals and some fassaite grains have small blebs of perovskite along their contacts with melilite. Some rhönite grains, like the one shown in Figure 2c, are associated with symplectic perovskite–fassaite–spinel intergrowths, as has been previously observed in other rhönite-bearing CTAs (El Goresy et al., 1977; Fuchs, 1978; Beckett, 1986). Perovskite also occurs as isolated grains up to ~ 70 μm across. Fremdlinge from A37, studied by Bischoff and Palme (1987), have cores of FeNi-metal, Pt-metal nuggets, W- and Mo-oxides, and V-rich magnetite, and rims of oxides and sulfides. Secondary alteration products are rare, as noted by Bischoff et al. (1987).

A brief description of Ef3 is given by Sylvester et al. (1993), who analyzed it by INAA and found that it has a group I REE pattern. In thin section it is 1.8×1.5 mm. Up to ~ 600 μm inward from the Wark–Lovering rim, spinel is nearly absent and melilite is virtually the only phase present. It occurs as prismatic grains ~ 70 μm across with many 120° triple junctions. Elsewhere in the inclusion, melilite occurs as laths up to 500 μm long and spinel is abundant, mainly occurring as euhedral grains, up to 100 μm across. Many spinel grains enclose perovskite and are themselves enclosed in melilite or, as in TS68, in rounded, anhedral 200–300- μm -sized fassaite grains. Fassaite also occurs in small, 20–50- μm interstitial pockets between melilite grains (Fig. 2d). Many 10–20- μm NiFe grains are present, and the inclusion also contains a large (~ 100 μm) Fremdling, consisting of kamacite, taenite, V-magnetite, and phosphate, which was described by Casanova and Grossman (1993).

Perhaps the most extreme example of concentration of spinel in the interior of an inclusion occurs in AX4 (Fig. 2e), a CTA from Axtell that was first described by Simon et al. (1994a). Up to ~ 1 mm inward from the Wark–Lovering rim, this sample is quite spinel-poor, consisting of subhedral melilite grains from 150 to 200 μm across, blebby perovskite grains up to 100 μm across, and patches of secondary anorthite (not shown) that are ~ 400 μm across. In the interior of the inclusion, however, the concentration of spinel is so high that the spinel grains are in contact with each other, and some areas are nearly monomineralic. The spinel occurs as subhedral to euhedral grains that are mostly between 10 and 100 μm across. Perovskite is also more abundant in the core of the inclusion than it is in the outer region, and in the spinel-rich area there are several places where spinel grains are completely enclosed in perovskite. Another CTA from Axtell, AX30, has a small spinel-perovskite-rich zone in its interior, somewhat similar to that in AX4. Sample AX30 is a lightly altered inclusion in which melilite is present as a mosaic of stubby, tabular grains that are mostly 50–100 μm across. Outside of the core, perovskite occurs as anhedral grains up to 50 μm across, and in small interstices between melilite crystals, in some cases outlining them (Fig. 2f).

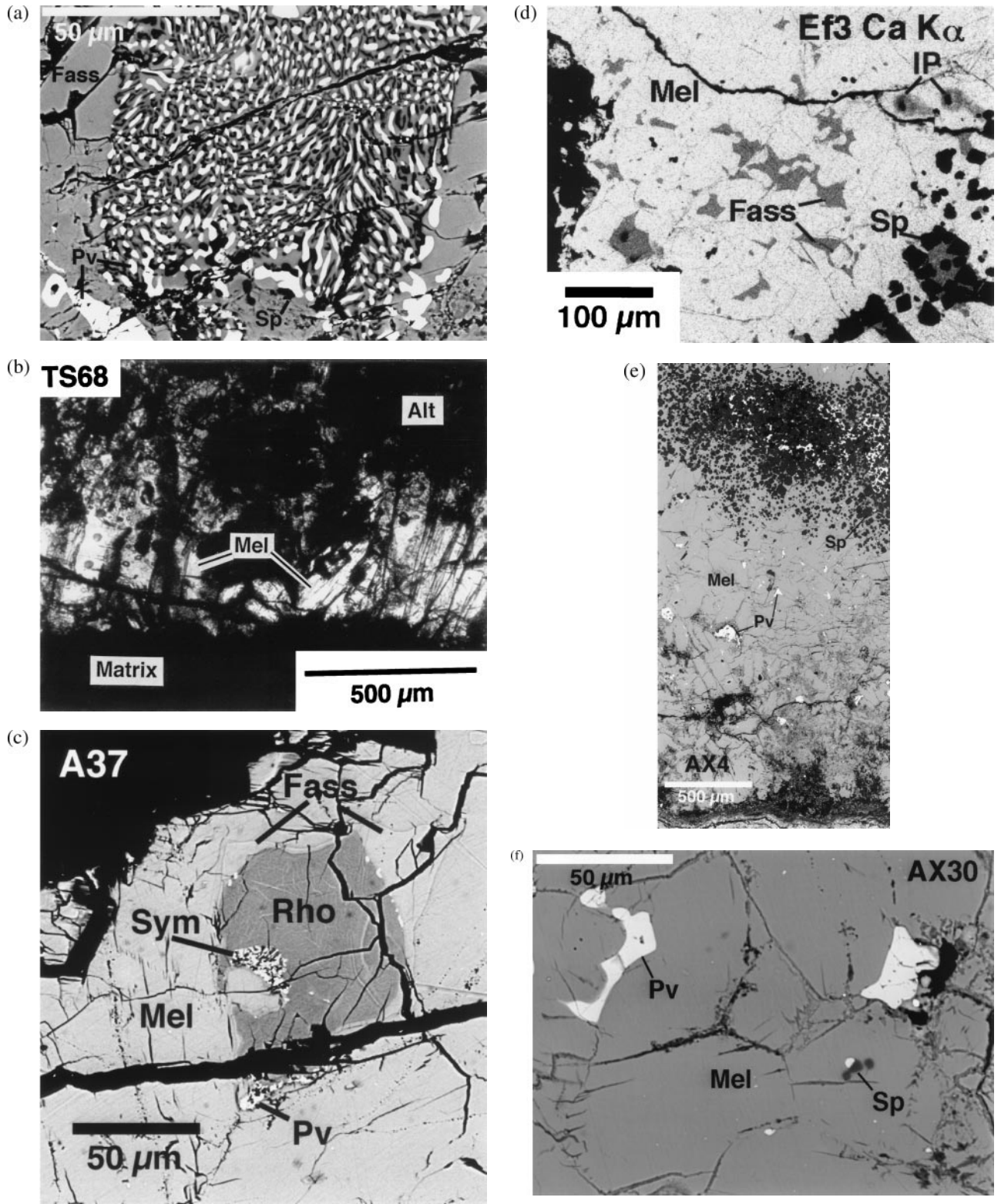


Fig. 2. Petrographic features of CTAs. (a) BEI of perovskite (Pv)-spinel (Sp)-fassaite (Fass) symplectite in TS32. (b) Transmitted plane-light photomicrograph of radially oriented melilite (white) adjacent to the rim of TS68. (c) BEI of a rhönite (Rho) grain and associated symplectite (Sym) and fassaite (Fass) in A37. Note tiny perovskite grains (bright) along the rhönite-fassaite contact. (d) CaK_α X-ray map showing the interstitial occurrence of fassaite in Ef3. Abbreviations as used previously (except IP: ion-probe spots). (e) BEI of AX4, showing its spinel-poor outer zone (lower half of image) and the spinel-perovskite-rich core (upper portion). (f) BEI of interstitial perovskite grains that crystallized around melilite crystals in AX30. Abbreviations as used previously.

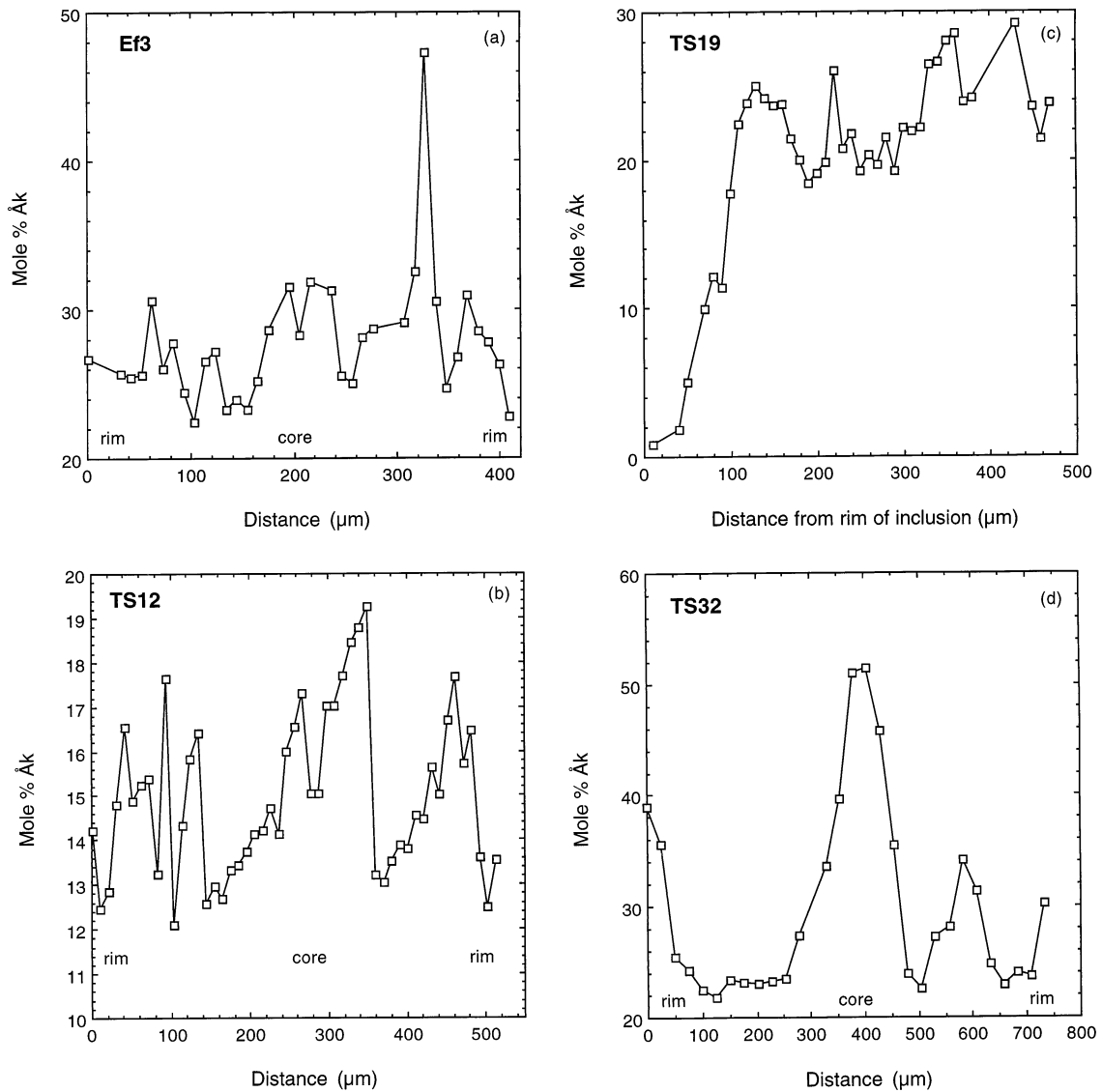


Fig. 3. Examples of zoning with respect to Åk content within single melilite crystals in CTAs. (a) Typical traverse with mostly small variations and no dominant trend. (b) Sawtooth zoning pattern in TS12. (c) Grain in TS19 showing a depletion in Åk adjacent to the rim of the inclusion. (d) A reversely zoned grain in TS32, with an Åk-rich core enclosed in relatively Åk-poor melilite.

3.3. Mineral Chemistry

3.3.1. Melilite

Whether a melilite crystal grows from a liquid of type A or type B composition or condenses as a solid from the solar nebular gas, its Mg content can be expected to increase with decreasing temperature. In most melilite grains in type B1 inclusions, Åk content varies regularly, gradually increasing with distance from the crystal core or, in the case of mantle grains, from the crystal rim nearest the inclusion margin. This is considered normal zoning. Reverse zoning is common in melilite in fluffy type A inclusions (MacPherson and Grossman, 1984). Many CTA melilite grains are unzoned, some are normally zoned, and some, in TS32 and USNM 3898 (Podosek et al., 1991), have reverse zoning. Results of electron micro-

probe traverses across four grains are illustrated in Figure 3. A common pattern (Fig. 3a) shows many small variations but no dominant trend. Most of the melilite in TS12 is homogeneous, with variations of only a few mol% Åk. Some grains in this inclusion, however, exhibit "sawtooth" patterns, with, as illustrated in Figure 3b, repeated sequences consisting of a gradual increase in Åk content up to a peak level, then a sharp decrease, then another gradual increase. TS19 contains normally zoned melilite, with Åk-poor cores and Åk-rich rims, and irregular, patchy-zoned melilite. Like that in TS2 (Simon et al., 1998), the relatively Åk-poor regions contain dispersed, micron-size spinel grains and the relatively Åk-rich regions do not. Unlike TS2, the shapes of the Åk-poor regions do not look like dendritic crystals. Nearly pure gehlenite occurs near the rim of the inclusion as shown by the results for a crystal that is in

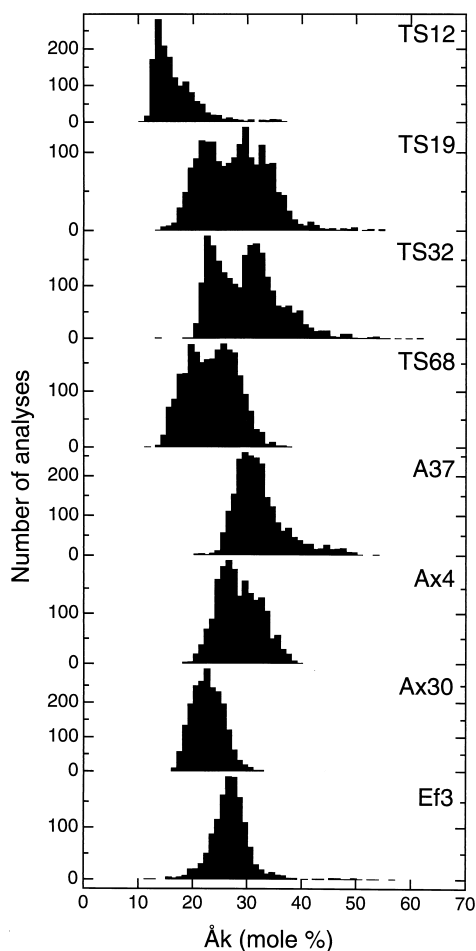


Fig. 4. Histograms of Åk contents of melilite from each inclusion studied. The inclusions show narrower ranges than is observed in melilite in type B1 inclusions. For each inclusion, 3072 analyses were collected in ~ 1 mm², yielding from 1355 (Ef3) to 2412 (TS32) stoichiometric melilite analyses per sample. Analyses have an uncertainty of ± 1 mol% Åk for each spot.

contact with the rim (Figure 3c). This pattern is qualitatively similar to some we have observed in TS68 rim melilites and in some type B1 mantle melilites (e.g., Davis et al., 1992). Some grains in TS32 are unzoned, and some are reversely zoned. A traverse across a reversely zoned grain in TS32 is illustrated in Figure 3d. It has an Åk-rich core, an Åk-poor mantle, and an Åk-rich rim.

To compare the populations of melilite in the samples, we obtained quantitative maps via EDS for each sample. The outermost rims of some CTAs contain hibonite, and, just underneath the W-L rim, nearly pure gehlenite is common. These phases are unlikely to have crystallized from melts of CTA compositions and probably formed in aluminous vaporization rinds (Beckett and Stolper, 1994). Because the near-rim melilite compositions probably are not primary, such regions were avoided during mapping. The results are illustrated in Figure 4. Two inclusions (AX30, Ef3) have symmetrical distributions of compositions about the mean, three (TS12, A37, AX4) have somewhat skewed distributions, two (TS19, TS68) have broad peaks or possibly bimodal distributions, and TS32 clearly has a

bimodal distribution. The latter pattern is not likely to have resulted from fractional crystallization. One of the peaks may reflect a relict grain population. TS12 has the most gehlenitic average melilite composition, Åk_{16.6}. Averages for the other inclusions range from Åk₂₃ (TS68, AX30) to Åk₃₂ (A37). The predominant lack of strong zoning of the melilite crystals is reflected in the generally narrow ranges seen for each inclusion. Compositions more magnesian than Åk₄₅ are rare, unlike type B1s, in which it is common to find melilite as magnesian as Åk₆₀ in crystal rims and in inclusion interiors.

3.3.2. Fassaite

The fassaite in CTAs exhibits some general similarities to that in type B inclusions, as well as some striking differences. Many fassaite in type B CAIs are continuously zoned from relatively Ti-, Sc-, V-rich, Mg-poor cores to Ti-, Sc-, V-poor, Mg-rich rims (e.g., Simon et al., 1991). In CTAs, the fassaite is quite rich in the compatible oxides and tends to be unzoned, although some grains have rims that are Ti-, Sc-poor relative to their cores. Representative analyses are given in Table 1 and all of our data are summarized in Figure 5. As illustrated in Figure 5a, CTA fassaite has higher Ti oxide and lower SiO₂ contents than that from type B inclusions. Except for a few analyses from TS68, there is no overlap between fassaite from CTAs and typical fassaite from type Bs. The anomalous fassaite found in the mantle of TS34, a type B1 from Allende (Simon et al., 1991), is so Ti-rich that it plots with the CTA fassaite, however, and not with the fassaite from type B inclusions.

Except for that in TS32, most CTA fassaite has between 0.2 wt% and 0.8 wt% Sc₂O₃ and the abundances are not correlated with Ti contents (Fig. 5b). In contrast, fassaite in type B CAIs, except for that in the mantle of TS34, generally has ≤ 0.25 wt% Sc₂O₃ and the abundances are correlated with Ti contents (Simon et al., 1991). The fassaite in TS32 is quite Sc₂O₃-rich, containing between 0.4 wt% and 2.0 wt%. All of the analyses of TS32 fassaite with >1.6 wt% Sc₂O₃ are from the same grain, which also has higher V₂O₃ contents than fassaite elsewhere in the inclusion (Fig. 5c). Most CTA fassaite has V₂O₃ contents between 0.1 wt% and 1.0 wt%, whereas type B fassaite mostly has ≤ 0.4 wt%. The fassaite in the CTAs we analyzed exhibits a wide range of V₂O₃/Sc₂O₃ ratios and reaches much higher V₂O₃ contents than does typical fassaite from type B inclusions. This is at least partially due to the fact that we analyzed V₂O₃-rich (>1 wt%) fassaite grains in TS68 and Ef3 that are near Fremdlinge, although some, like the V-rich grains from the mantle of TS34, occur as small, isolated grains in melilite. Within fassaite from a given CTA, V₂O₃ and Sc₂O₃ are generally correlated with each other, albeit with some scatter, as in fassaite in type B inclusions.

3.3.3. Spinel

The spinel grains in CTAs, like those of type B inclusions, are unzoned and are near-end-member MgAl₂O₄. Unaltered spinel is virtually FeO-free. Minor oxides present include Cr₂O₃ (0.1–0.5 wt%), TiO₂ (mostly 0.2–1.0 wt%), although values up to 2.2 wt% were found in TS12) and V₂O₃. The abundances of TiO₂ and V₂O₃ in CTA spinel are summarized in Figure 6. With one exception, the CTAs in our suite have

Table 1. Electron microprobe analyses of fassaite in compact type A inclusions.

| | TS32 | | | TS68 | | A37 | | Ef3 | |
|---------------------------------|--------|--------|--------|--------|--------|-------|--------|--------|-------|
| | 1 | 2 | 3 | 1 | 2 | 1 | 2 | 1 | 2 |
| MgO | 7.09 | 7.36 | 6.30 | 5.72 | 6.69 | 6.67 | 7.08 | 5.82 | 6.46 |
| Al ₂ O ₃ | 18.45 | 17.62 | 18.51 | 20.47 | 20.12 | 18.67 | 18.78 | 19.92 | 19.47 |
| SiO ₂ | 31.84 | 34.01 | 31.66 | 30.87 | 32.22 | 32.18 | 32.75 | 31.07 | 31.70 |
| CaO | 24.62 | 24.73 | 24.86 | 24.59 | 24.63 | 24.42 | 24.56 | 24.56 | 24.55 |
| Sc ₂ O ₃ | 0.62 | 1.20 | 1.84 | 0.56 | 0.12 | 0.45 | 0.43 | 0.40 | 0.56 |
| TiO ₂ ^{tot} | 17.96 | 15.77 | 17.27 | 18.37 | 16.75 | 18.04 | 17.46 | 18.94 | 17.58 |
| V ₂ O ₃ | 0.19 | 0.08 | 0.67 | 0.72 | 0.59 | 0.22 | 0.13 | 0.55 | 0.53 |
| FeO | BLD | BLD | BLD | BLD | 0.06 | BLD | BLD | BLD | 0.09 |
| ZrO ₂ | 0.44 | 0.51 | 0.46 | 0.12 | 0.14 | 0.25 | 0.23 | 0.13 | 0.14 |
| Ti ₂ O ₃ | 10.38 | 10.42 | 11.19 | 12.05 | 10.10 | 11.64 | 10.75 | 12.67 | 10.89 |
| TiO ₂ | 6.51 | 4.26 | 5.05 | 5.07 | 5.54 | 5.14 | 5.52 | 4.96 | 5.54 |
| Total | 100.14 | 100.19 | 100.54 | 100.17 | 100.21 | 99.64 | 100.23 | 100.08 | 99.93 |
| Cations per 6 oxygen anions | | | | | | | | | |
| Si | 1.215 | 1.292 | 1.214 | 1.181 | 1.221 | 1.232 | 1.241 | 1.190 | 1.211 |
| Al | 0.785 | 0.708 | 0.786 | 0.819 | 0.779 | 0.768 | 0.759 | 0.810 | 0.789 |
| Tet. sum | 2.000 | 2.000 | 2.000 | 2.000 | 2.000 | 2.000 | 2.000 | 2.000 | 2.000 |
| Al | 0.046 | 0.081 | 0.051 | 0.103 | 0.120 | 0.074 | 0.080 | 0.090 | 0.087 |
| Mg | 0.404 | 0.417 | 0.360 | 0.326 | 0.378 | 0.380 | 0.400 | 0.332 | 0.368 |
| Ca | 1.000 | 1.000 | 1.000 | 1.000 | 1.000 | 1.000 | 1.000 | 1.000 | 1.000 |
| Sc | 0.021 | 0.040 | 0.062 | 0.019 | 0.004 | 0.015 | 0.014 | 0.013 | 0.019 |
| Ti ³⁺ | 0.330 | 0.329 | 0.355 | 0.383 | 0.319 | 0.372 | 0.340 | 0.405 | 0.346 |
| Ti ⁴⁺ | 0.186 | 0.121 | 0.144 | 0.145 | 0.158 | 0.148 | 0.158 | 0.142 | 0.159 |
| V | 0.005 | 0.002 | 0.019 | 0.021 | 0.017 | 0.006 | 0.004 | 0.016 | 0.015 |
| Fe | 0 | 0 | 0 | 0 | 0.002 | 0 | 0 | 0 | 0.003 |
| Zr | 0.008 | 0.010 | 0.009 | 0.002 | 0.002 | 0.005 | 0.004 | 0.002 | 0.003 |
| Oct. sum | 2.000 | 2.000 | 2.000 | 1.999 | 2.000 | 2.000 | 2.000 | 2.000 | 2.000 |

BLD: Below detection limit of electron microprobe of 0.041 wt% FeO. Analyses are normalized to four cations, including two tetrahedral cations and one Ca cation, per six O anions, according to the methods of Beckett (1986).

spinel with 0.2–1.4 wt% V₂O₃, with most abundances between 0.4 and 1.2 wt% (Fig. 6). The exception is AX30, in which the spinel has from 2 wt% to 4.6 wt% V₂O₃. Note the fairly narrow range of V₂O₃ contents of spinel within each sample, again with the exception of AX30. The present results contrast with those of MacPherson and Grossman (1984), who found that the spinel of fluffy type A inclusions tends to be V₂O₃-rich (>~1.5 wt% V₂O₃), with ranges of 2–3 wt% within individual samples.

3.3.4. Perovskite

In most CTAs, this phase is nearly end-member CaTiO₃, with minor (<0.5 wt%) contents of Al₂O₃, SiO₂, and V₂O₃. Oxides of the rare-earth elements and Y can also reach levels between 0.1 wt% and 0.5 wt%, as in the REE-rich perovskite in TS12 (Laughlin et al., 1986). Perovskite in the present samples contains between several hundred and several thousand ppm Nb, but not the wt% levels seen in some perovskite from Allende CTA TS2 (Simon et al., 1998).

3.3.5. Rhönite

One member of our suite, A37, contains rhönite, a complex solid solution of at least eight chemical components (Beckett, 1986), with the general formula Ca₄(Ca, Fe, Mg, Al, V, Ti)₁₂(Al, Si)₁₂O₄₀. Representative analyses are given in Table 2. Despite the wide range of possible compositions, the abundances of the major element oxides in A37 rhönite fall within

a fairly narrow composition range. The Allende rhönite analysis given by Fuchs (1978) is within the range of the A37 rhönite, but that analyzed by Fuchs (1971) has slightly higher MgO, Al₂O₃, SiO₂, and CaO contents and lower TiO₂^{tot} contents. Mason and Taylor (1982) reported rhönite containing ~3 wt% V₂O₃, but the abundances of the other oxides are similar to those reported here.

3.4. Trace-Element Abundances

Bulk trace-element analyses, obtained by instrumental neutron activation analysis, are available for six of the samples in our suite. Such data are helpful in the interpretation of the ion-microprobe analyses of individual phases. Four of the inclusions have flat CI-normalized REE patterns with abundances of the trivalent REE at 16–20 × CI and small, positive Eu anomalies. These inclusions are TS12 (Grossman and Ganapathy, 1976), A37 (Bischoff et al., 1987), Ef3 (Sylvester et al., 1993), and AX4 (Yoneda et al., 1995). Inclusion TS19 has an unusual pattern, with light REE (LREE) abundances of 8–10 × CI, a positive Eu anomaly, and a depletion in Dy relative to Tb and Yb (Grossman and Ganapathy, 1976). Axtell inclusion AX30 also has low LREE abundances (~6–10 × CI), a positive Eu anomaly, and depletions of the refractory heavy REE (HREE) relative to the LREE. This pattern was classified by Yoneda et al. (1995) as a modified group II pattern (Martin and Mason, 1974). A CTA from Allende, TS2, also has a group

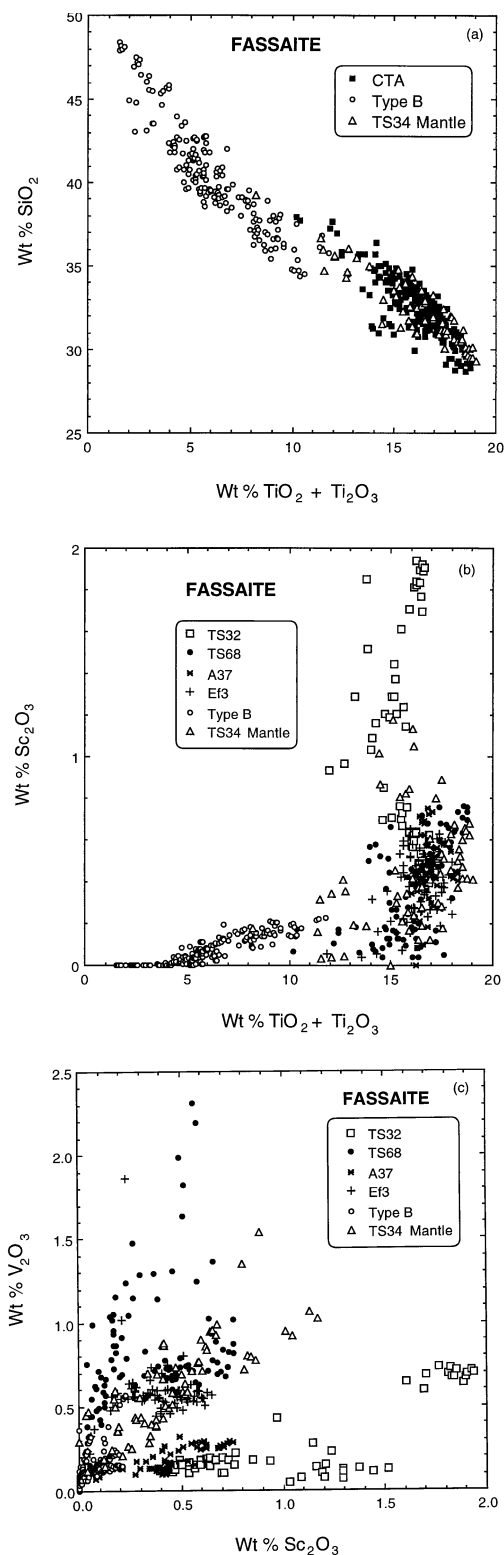


Fig. 5. Oxide relationships in fassaite. (a) SiO₂ vs. TiO₂ + Ti₂O₃ for fassaite from CTAs, type B inclusions, and the mantle of Allende type B1 inclusion TS34. For these oxides, there is much overlap among analyses from different CTAs, so in this plot one symbol is used for all CTA fassaite analyses. (b) Sc₂O₃ vs. Ti oxides. Fassaite in CTAs tends to have higher Sc₂O₃ contents than fassaite from type B inclusions. (c) V₂O₃ vs. Sc₂O₃. These oxides are positively correlated, but the V₂O₃/Sc₂O₃ ratio varies from inclusion to inclusion.

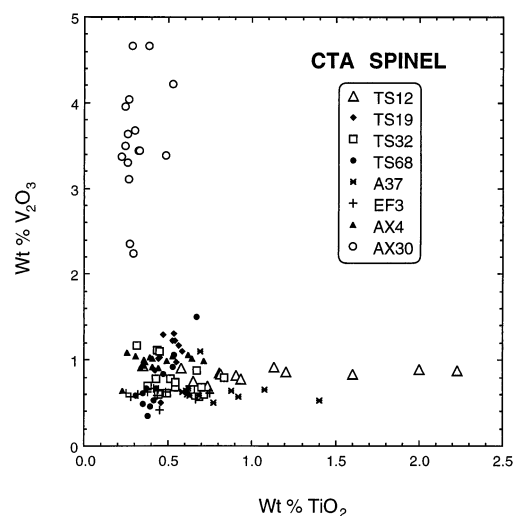


Fig. 6. Plot of V₂O₃ vs. TiO₂ abundances in CTA spinel. Contents of V₂O₃ are fairly uniform within each inclusion, except AX30.

II-like bulk REE pattern (Simon et al., 1998), but such patterns are rare among coarse-grained inclusions.

Phases in six of the samples we studied were analyzed by ion microprobe. Results for the REE and Y are summarized in Figure 7 and analyses of fassaite and rhönite are presented in Table 3. Melilite is fairly uniform within each inclusion, so only averages are shown. In TS12, TS32, A37, Ef3, and AX4 the melilite patterns are flat with small, positive Eu anomalies. In TS68 the HREE decrease from Gd through Lu. Fassaite in

Table 2. Electron microprobe analyses of rhönite in A37.

| | 1 | 2 | 3 |
|---------------------------------|--------|--------|--------|
| MgO | 18.41 | 17.87 | 18.26 |
| Al ₂ O ₃ | 26.47 | 27.15 | 26.49 |
| SiO ₂ | 17.47 | 17.81 | 18.61 |
| CaO | 14.80 | 15.24 | 14.99 |
| TiO ₂ ^{tot} | 22.06 | 21.24 | 20.81 |
| Sc ₂ O ₃ | 0.35 | 0.32 | 0.38 |
| V ₂ O ₃ | 0.82 | 0.73 | 0.78 |
| FeO | 0.05 | 0.41 | 0.19 |
| Ti ₂ O ₃ | 7.64 | 7.40 | 7.83 |
| TiO ₂ | 13.57 | 13.02 | 12.12 |
| Total | 99.58 | 99.95 | 99.65 |
| Cations per 40 oxygen anions | | | |
| Si | 4.467 | 4.536 | 4.744 |
| Al | 7.533 | 7.464 | 7.256 |
| Tet. sum | 12.000 | 12.000 | 12.000 |
| Al | 0.443 | 0.689 | 0.705 |
| Mg | 7.015 | 6.785 | 6.937 |
| Ca | 4.055 | 4.160 | 4.095 |
| Ti ³⁺ | 1.633 | 1.576 | 1.667 |
| Ti ⁴⁺ | 2.610 | 2.494 | 2.323 |
| Sc | 0.078 | 0.070 | 0.085 |
| V | 0.157 | 0.140 | 0.149 |
| Fe | 0.011 | 0.088 | 0.040 |
| Sum | 16.002 | 16.002 | 16.001 |
| Total cations | 28.002 | 28.002 | 28.001 |

Analyses are normalized to 28 cations, including 12 tetrahedral cations, per 40 oxygen anions.

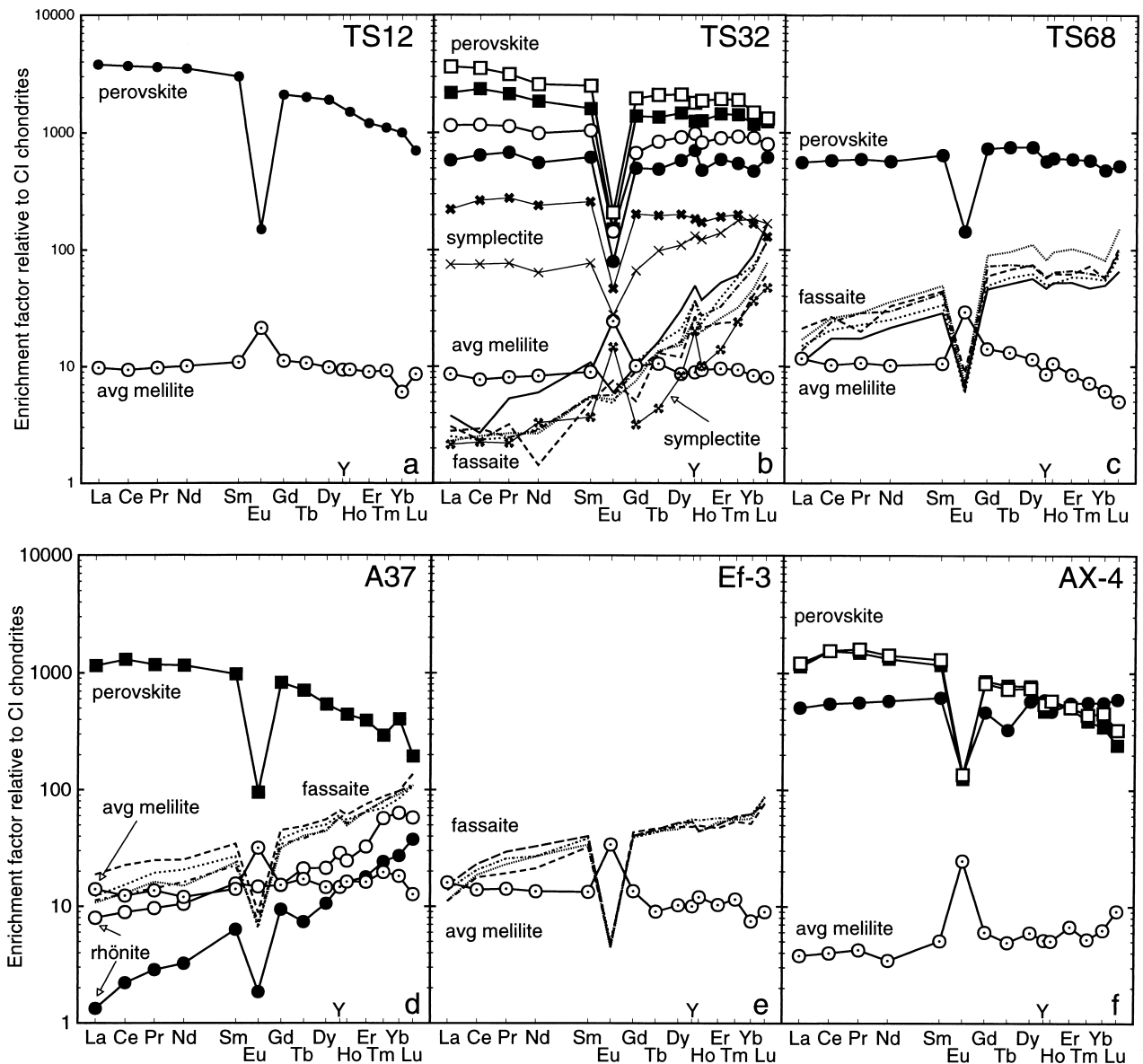


Fig. 7. Chondrite-normalized REE patterns of phases in CTAs, determined by ion microprobe. Within each inclusion, the melilite compositions are rather homogeneous, so only averages are shown. (a) TS12. (b) TS32. (c) TS68. (d) A37. (e) Ef3. (f) AX4.

the latter two inclusions and A37 has chondrite-normalized REE patterns similar to fassaite from type B1 inclusions (Simon et al., 1991), with increasing abundances from La through Lu and large, negative Eu anomalies. The fassaite in TS32, however, is distinctive, with uniform abundances from La through Pr and sharp increases from Nd through Lu with no Eu anomaly. It is quite unusual for extraterrestrial pyroxene to lack a negative Eu anomaly, because the relatively large Eu^{2+} cation is too large for any of the crystallographic sites in pyroxene. Rhönite (in A37) has low REE abundances with $\text{HREE} > \text{LREE}$, and >2000 ppm of Sc and of V.

Perovskite exhibits a wide range of trivalent REE contents, from 500 to $\sim 4000 \times \text{CI}$. In all samples, perovskite has flat or LREE-enriched patterns with large, negative Eu anomalies. A wide range of REE abundances is also seen in analyses of

symplectites in TS32, which are also illustrated in Figure 7. This probably reflects sampling of different proportions of phases during the analysis of these fine-grained intergrowths.

4. DISCUSSION—FORMATION OF COMPACT TYPE AS

4.1. Volatilization Residues

Compact type A inclusions either formed by volatilization of less refractory material, crystallization of liquids, gas–solid condensation, or by some combination of these processes. Using our data and observations and those in the literature, we can evaluate these possibilities.

An early suggestion was that CAIs, including CTAs, were volatilization residues of chondritic material (e.g., Kurat, 1970,

Table 3. Representative ion probe analyses of fassaite and rhönite in CTAs.*

| | 1 | 2 | 3 | 4 | 5 | 6 |
|------------------------------------|-------------|---------------|-------------|-------------|-------------|--------------|
| MgO (%) | 7.2 | 5.8 | 6.4 | 7.0 | 14.9 | 12.0 |
| Al ₂ O ₃ (%) | 16.8 | 17.4 | 19.2 | 16.5 | 27.2 | 25.1 |
| SiO ₂ (%) | 34.0 | 32.4 | 29.1 | 35.4 | 18.3 | 15.2 |
| CaO (%) | 24.9 | 24.8 | 24.5 | 25.1 | 13.8 | 20.5 |
| TiO ₂ (%) | 15.4 | 16.6 | 19.7 | 15.2 | 24.4 | 22.1 |
| Li | 0.04 ± 0.01 | 0.02 ± 0.01 | 0.04 ± 0.02 | 0.05 ± 0.02 | 6.16 | 0.52 ± 0.08 |
| Be | 0.45 ± 0.03 | 0.38 ± 0.03 | 0.42 ± 0.08 | 0.34 ± 0.06 | 0.96 ± 0.14 | 0.84 ± 0.13 |
| B | 9.2 | 7.53 | <0.20 | <0.20 | <0.20 | 0.93 ± 0.23 |
| F | 23.5 ± 3.7 | 14.0 ± 2.9 | 34.1 ± 9.5 | 41 ± 12 | <13.5 | 112.4 ± 20.9 |
| Na | 135 | 69.2 | 27.8 | 51.2 | 23.5 | 189.5 |
| P | <16 | <14.6 | 60.8 ± 5.9 | <17.4 | 31.5 ± 5.2 | 82.3 ± 8.4 |
| Sc | 3742 | 11166 | 3791 | 606 | 2531 | 2046 |
| V | 831 | 4098 | 1243 | 2545 | 4148 | 2822 |
| Cr | 357 | 363 | 208 | 178 | 678 | 684 |
| Co | 151 | 101 | 10.3 ± 1.9 | 22.7 ± 2.8 | 8.6 ± 1.9 | 127 |
| Fe | 727 ± 84 | 348 ± 71 | 536 ± 101 | 315 ± 84 | 295 ± 68 | 31521 |
| Ni | 3975 | 1665 | <20.2 | <24 | 75 ± 10 | 170 ± 24 |
| Rb | 8.65 ± 0.52 | 18.7 | 4.97 ± 0.60 | 1.69 ± 0.34 | 1.80 ± 0.54 | 3.18 ± 0.65 |
| Sr | 81.8 | 73.8 | 63.3 | 65.6 | 31.2 | 114.3 |
| Y | 56.0 | 39.4 | 92.2 | 125 | 22.5 | 43.6 |
| Zr | 2400 | 2695 | 1404 | 850 | 243 | 255.1 |
| Nb | 2.81 ± 0.22 | 6.03 ± 0.33 | 5.10 ± 0.38 | 5.6 ± 0.4 | 7.58 ± 0.57 | 12.3 ± 0.7 |
| Cs | 0.30 ± 0.11 | 0.53 ± 0.15 | 0.52 ± 0.17 | 0.16 ± 0.12 | 0.42 ± 0.19 | 1.01 ± 0.29 |
| Ba | 2.90 ± 0.26 | 3.51 ± 0.29 | 1.85 ± 0.24 | 1.29 ± 0.24 | 2.27 ± 0.32 | 45.42 |
| La | 0.59 ± 0.05 | 0.54 ± 0.05 | 2.87 ± 0.10 | 4.01 ± 0.14 | 0.31 ± 0.04 | 1.89 ± 0.10 |
| Ce | 1.43 ± 0.12 | 1.52 ± 0.13 | 9.23 | 15.7 | 1.33 ± 0.13 | 5.38 |
| Pr | 0.22 ± 0.06 | 0.24 ± 0.07 | 1.73 ± 0.16 | 2.58 ± 0.23 | 0.25 ± 0.07 | 0.86 ± 0.14 |
| Nd | 1.32 ± 0.25 | 1.20 ± 0.24 | 9.33 ± 0.60 | 16.3 ± 0.9 | 1.46 ± 0.29 | 4.74 ± 0.52 |
| Sm | 0.79 ± 0.09 | 0.81 ± 0.09 | 3.96 ± 0.22 | 7.28 ± 0.27 | 0.93 ± 0.13 | 2.31 ± 0.22 |
| Eu | 0.27 ± 0.03 | 0.29 ± 0.03 | 0.36 ± 0.03 | 0.41 ± 0.04 | 0.10 ± 0.02 | 0.83 ± 0.07 |
| Gd | 2.13 ± 0.24 | 1.47 ± 0.21 | 7.46 ± 0.45 | 17.7 | 1.85 ± 0.26 | 2.99 ± 0.39 |
| Tb | 0.57 ± 0.07 | 0.50 ± 0.06 | 1.65 ± 0.11 | 3.51 ± 0.18 | 0.27 ± 0.06 | 0.77 ± 0.10 |
| Dy | 5.07 ± 0.30 | 3.71 ± 0.26 | 12.19 | 26.9 | 2.57 ± 0.24 | 5.18 ± 0.35 |
| Ho | 1.30 ± 0.12 | 1.11 ± 0.11 | 3.06 ± 0.17 | 5.33 | 0.90 ± 0.11 | 1.37 ± 0.14 |
| Er | 6.19 | 4.14 ± 0.21 | 10.23 | 16.3 | 2.84 ± 0.20 | 5.17 ± 0.27 |
| Tm | 1.41 ± 0.08 | 0.78 ± 0.06 | 1.69 ± 0.08 | 2.25 ± 0.11 | 0.58 ± 0.06 | 1.38 ± 0.09 |
| Yb | 12.0 | 7.57 | 13.74 | 13.2 | 4.43 ± 0.31 | 10.31 |
| Lu | 2.85 | 1.89 ± 0.11 | 2.61 | 3.68 | 0.91 ± 0.08 | 1.41 ± 0.10 |
| Hf | 48 | 101 | 39.71 | 17.0 | 8.76 | 6.40 ± 0.36 |
| Th | <0.034 | <0.048 | 0.07 ± 0.03 | 0.18 ± 0.05 | <0.05 | <0.04 |
| U | <0.022 | 0.057 ± 0.025 | <0.034 | <0.034 | 0.16 ± 0.05 | 0.16 ± 0.05 |

Note: 1,2: Fassaite, TS32; 3: fassaite, A37; 4: fassaite, TS68; 5,6: rhönite, A37. A small metal grain was encountered in #6, causing elevated levels of Fe, Ni, and probably Co in the analysis.

* Results in parts per million unless otherwise indicated. Uncertainties are $\pm 1\sigma$ and upper limits are $<2\sigma$, based on counting statistics. Uncertainties are only given where they exceed 5% (relative).

1975). Beckett (1986) and Sylvester et al. (1993), however, showed that CTAs have superchondritic CaO/Al₂O₃ ratios. As pointed out by Beckett (1986), this is a feature not expected for vaporization residues, because CaO is less refractory than Al₂O₃. Beckett (1986) further reasoned that to make CTAs by evaporation and match their observed isotopic composition, $\delta^{30}\text{Si} \sim 2.5\%$ (Molini-Velsko, 1983), a starting composition with 60–80 wt% SiO₂ would be required. Finally, evaporation experiments performed by Floss et al. (1996) on bulk Allende powder showed that this process can yield phases, such as hibonite, that are found in some refractory inclusions (Floss et al., 1996), but melilite was not present in any of the residues; MgO and SiO₂ were either completely lost, or, where MgO and SiO₂ were retained, olivine and glass were present. Formation of CTAs by evaporation of chondritic material can therefore be ruled out. Evaporation of nonchondritic material is poorly constrained and cannot be ruled out as a mechanism for the

formation of CTAs, but this process would require a special starting composition unlike any observed, which, upon evaporation, would enter simultaneously the bulk chemical and isotopic composition range of CTAs.

4.2. Crystallization from Liquids vs. Condensation from a Gas

Two sets of experiments have been performed on type A bulk compositions to investigate whether these inclusions could have crystallized from liquids. Paque and Stolper (1984) performed controlled cooling experiments in air on a “melilite-rich B1” composition based on USNM 3898, an inclusion that is actually a CTA, as it contains 75% melilite and has rhönite and very Ti-rich fassaite (Mason and Taylor, 1982; Podosek et al., 1991). Paque and Stolper (1984) found the crystallization sequence of that composition to be spinel first, followed closely

by melilite, and then, after cooling by more than 200°C, late anorthite and perovskite. Primary anorthite is not found in CTAs, but its crystallization may have been suppressed, as in type B1s (MacPherson et al., 1984), due to moderately rapid cooling. Beckett (1986) performed isothermal melting experiments at an f_{O_2} of $\sim 10^{-8}$ atm on one composition corresponding to a fluffy type A inclusion and, in air, on one corresponding to a compact type A. He found, for both compositions, that melilite crystallized first, followed within $\sim 20^\circ\text{C}$ by spinel, and finally perovskite, at temperatures $\sim 150^\circ\text{C}$ below the appearance of spinel. Thus, both studies found nearly simultaneous onset of melilite and spinel crystallization, persistence of this assemblage over a temperature interval of 150°C – 200°C , and no fassaite crystallization. Both studies were carried out at high oxygen fugacities, however, and it is possible that lower oxygen fugacities would have stabilized Ti^{3+} -bearing fassaite relative to perovskite. So, even though no fassaite was produced in these experiments, and primary anorthite is not found in CTAs, these studies cannot be used to rule out formation of CTAs by crystallization from liquids.

Comparison of observed textures and assemblages with those predicted for fractional crystallization is probably not the best way to evaluate whether the observed features of CTAs are consistent with crystallization from liquids. Although the long intervals of melilite \pm spinel crystallization seen in experiments on type A compositions are consistent with the observations of high abundances of melilite in CTAs, it would be impractical to collect the experimental data needed to predict whether, in a given CTA, fassaite, perovskite, rhönite, or fassaite + perovskite, etc., should follow melilite + spinel for each of the members of our suite of CTAs. To do so would require accurate bulk composition determinations and experiments at solar f_{O_2} on each inclusion composition, with the assumption that the last liquids in the experiments behave the same as they did in the natural samples.

A test we can apply with more confidence is to see whether trace-element distributions among the minerals within a given inclusion are consistent with crystal/liquid fractionation. Partition coefficients (D s) for many elements have been measured for melilite (Kuehner et al., 1989; Beckett et al., 1990; Davis et al., 1996), fassaite (Simon et al., 1991), and perovskite (Kennedy et al., 1994), mostly in melts approximating type B inclusion compositions. If we assume that these D s are applicable to CTA compositions, we can address the first-order question of whether the trace-element contents of the phases in the present samples are consistent with partitioning during fractional crystallization.

To do this, we used simple fractional crystallization models for each of the CTAs for which sufficient trace-element data are available. We used inclusion bulk compositions as determined by INAA, which are presumably representative of the samples, in the models. Alternatively, we could have attempted to calculate bulk compositions from modal abundances and average phase compositions. In some cases, however, we would not be likely to calculate an accurate average composition of perovskite. Because of the wide range of REE contents observed in this phase, determination of a well-defined average might require more contamination-free analyses than could be obtained in some cases, due to perovskite's generally fine grain size. Due to the high REE content of perovskite, an inaccuracy in the

calculation of its average composition or its modal abundance would have a large effect on the calculated bulk composition.

The models start with crystallization of the amount of spinel observed, assuming $D_{\text{REE}}^{\text{Sp/Liq}} = 0$, from the bulk composition. This is followed by crystallization of the amount of melilite needed to fractionate the liquid to the point that fassaite or perovskite, whichever is found in the inclusion being modeled, would crystallize with the observed La content. In cases where there were only trace amounts of these phases, this required virtually all of the melilite to precede the late phase rather than cocrystallize with it, whereas those inclusions, such as TS68 and Ef3, that contain significant (~ 15 vol%) amounts of fassaite, require less fractionation. The correlation between observation and calculation supports the validity of the application of this approach to these samples.

For each inclusion, the D used for partitioning of the trivalent REE between melilite and liquid was that calculated using the relationship:

$$D_{\text{REE}}^{\text{mel/liq}} = K(X_{\text{Ge}}/X_{\text{Ak}})$$

The average Ge/Åk ratio from the electron probe analyses was used, and values of K were taken from Simon et al. (1994b), who calculated them from the experimental results of Kuehner et al. (1989). We assumed that $D_{\text{Eu}} \cong D_{\text{Sr}}$ and used a value of 0.8 for $D_{\text{Eu}}^{\text{mel/liq}}$ (Kuehner et al., 1989).

4.2.1. TS12

For TS12, bulk INAA (Grossman and Ganapathy, 1976) and RNAA data (Grossman et al., 1977) along with modal mineralogy (Beckett, 1986) are available. We assumed that the first perovskite to crystallize after melilite is relatively REE-rich and is represented by the ion probe analysis of REE-rich perovskite in Laughlin et al. (1986). In modeling the fractional crystallization of this inclusion, we started with the bulk composition, C_{O} , and calculated C_{L} , the residual liquid composition, after crystallization of 8% spinel (Beckett, 1986) using the relationship:

$$C_{\text{L}} = C_{\text{O}}F^{(D-1)}$$

where F is the proportion of liquid remaining. The resulting C_{L} for La, 4.73 ± 0.10 ppm, was used as a new C_{O} for the beginning of melilite crystallization. The value of C_{L} at the onset of perovskite crystallization was set to 93.88 ppm, the La content of a residual liquid that would yield perovskite with the observed 892 ppm (Laughlin et al., 1986), assuming a $D_{\text{La}}^{\text{pv/l}} of 9.5$ (Kennedy et al., 1994). From the aforementioned values of C_{L} and C_{O} and the D for the average melilite composition, Åk₁₅, the Rayleigh equation was used to calculate F , the amount of liquid remaining at the onset of perovskite crystallization. This value of F was then used to calculate C_{L} for the other REE determined by INAA (Ce, Sm, Eu, Tb, Dy, Yb) and RNAA (Lu), from which the corresponding concentrations in perovskite could be obtained. The results of this calculation and those for the other CTAs we modeled are illustrated in Figure 8.

For TS12 (Fig. 8a) a fairly good match, except for Dy and Lu, was obtained between the calculated REE abundances and those observed in the REE-rich (presumably early) perovskite.

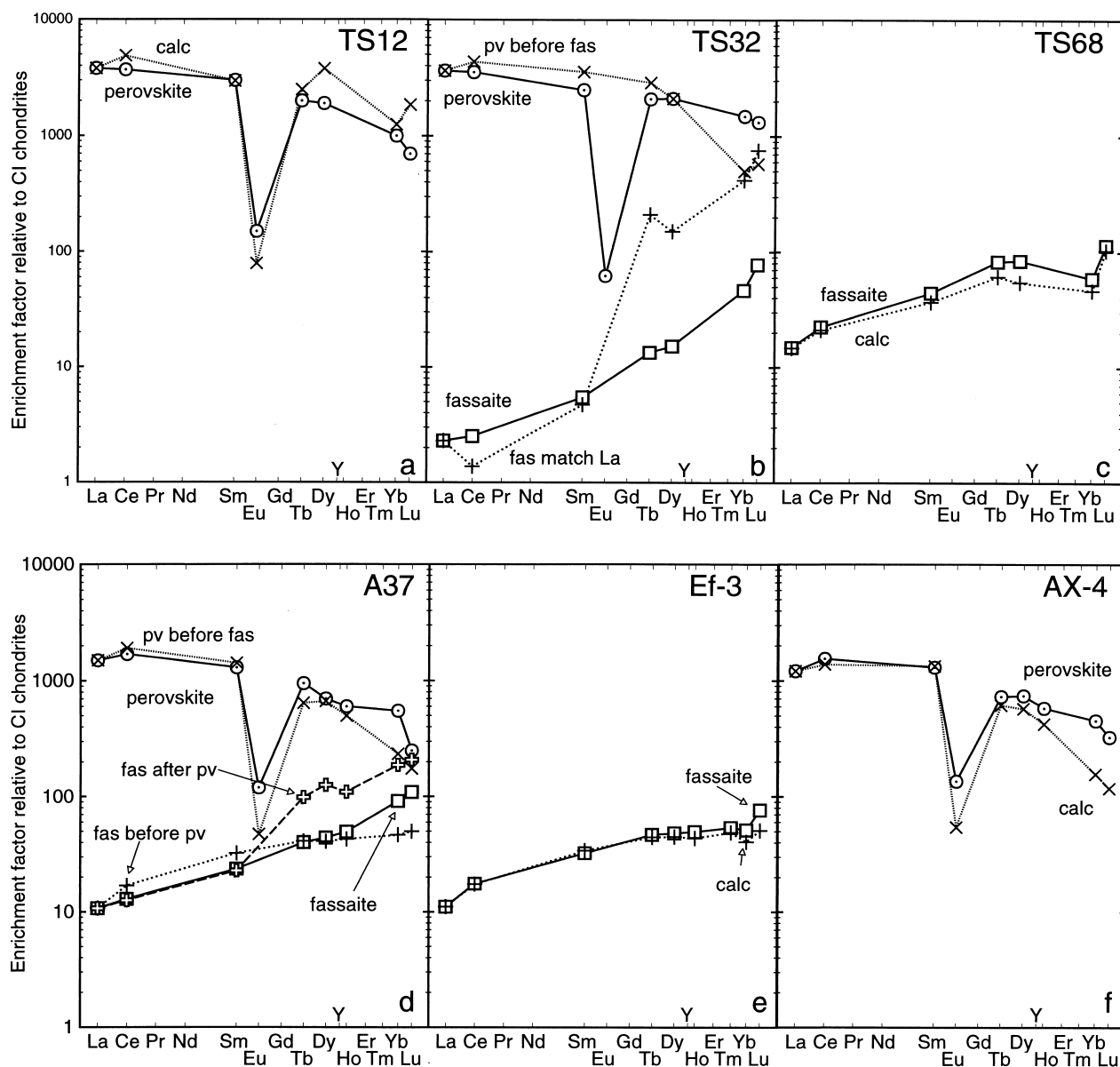


Fig. 8. Comparison of chondrite-normalized REE abundances of phases observed in CTAs with patterns predicted for those phases if they formed by fractional crystallization. Where there is agreement between observed and calculated results, the measurements are consistent with formation of the inclusion by crystallization of a liquid. Ion-probe analyses are labeled by phase, calculated patterns by "calc" or by crystallization sequence, such as "pv before fas" for crystallization of perovskite before fassaite. (a) TS12, perovskite. (b) TS32; "fas match La": model in which some perovskite is crystallized so that fassaite crystallizes with the observed La content. (c) TS68, fassaite. (d) A37; "fas after pv": matching the observed La content of fassaite, with prior crystallization of perovskite. (e) Ef3, fassaite. (f) AX4, perovskite.

The discrepancy between the observed and calculated Dy abundances may reflect a problem with the INAA data, because, in that analysis (Grossman and Ganapathy, 1976), $Dy/Tb \sim 1.2 \pm 0.1 \times CI$ but, in ion-probe analyses of melilite and perovskite from this inclusion, $Dy/Tb < 1 \times CI$. The disagreement between calculated and observed Lu abundances cannot be readily accounted for, however. Both the bulk composition and the ion-probe analyses of melilite have $Lu/Yb > 1 \times CI$. We would, therefore, expect to see a superchondritic Lu/Yb ratio in perovskite as well, as shown in Figure 8a, because $D_{Yb}^{pv/liq}$ is only slightly larger than $D_{Lu}^{pv/liq}$ (Kennedy et al., 1994). Ion-

probe analyses of perovskite in TS12 have subchondritic Lu/Yb ratios, however.

This modeling method is very sensitive to the melilite composition used because the D s for the trivalent REE vary with $\text{\AA}k$ content (Kuehner et al., 1989; Beckett et al., 1990). It has the advantage, however, of avoiding a dependency on an accurate model of the relationship between the degree of liquid crystallization and the corresponding melilite composition (mol% $\text{\AA}k$), which has been elusive in the modeling of the trace-element abundances of melilite in Bls (e.g., Davis et al., 1992; Simon et al., 1994b).

Nevertheless, we also tried a model in which a linear F vs. $\dot{A}k$ relationship was calculated as in Davis et al. (1992) and the $D_{\text{REE}}^{\text{mel/liq}}$ varied accordingly, to see if this provided a better fit to the data than modeling with the average melilite composition (or average $D_{\text{REE}}^{\text{mel/liq}}$). We found that, at least in the case of TS12, the two models provide equally good fits to the data, and, except for Ce and Eu, either match or bracket the observed abundances. Therefore, for the remaining samples, only the “average D ” model was used.

Simon et al. (1994b) calculated the chondrite-normalized REE pattern for perovskite crystallized from a type A inclusion composition after crystallization of 15% spinel and 77% melilite. Their pattern, strongly reflecting the perovskite/liquid D s, is very similar to the pattern of the perovskite in TS12 (Fig. 7a); that is, high, very gently sloping LREE abundances; a deep negative Eu anomaly; and HREE abundances that are lower than those of the LREE, and which decrease from Gd through Lu. From our observations and calculations, and those of Simon et al. (1994b), we conclude that TS12 crystallized from a melt.

4.2.2. TS32

There are no INAA data for this inclusion, so for its bulk composition we used the average of the other four Allende CTAs considered here. For La, this gave 3.58 ± 0.80 ppm, or $\sim 15 \times \text{CI}$. In the model, 2.2% spinel was crystallized first, followed by the 96.5% of the inclusion that consists of melilite and alteration products (Beckett, 1986). This inclusion has minor amounts of both perovskite and fassaite, either of which could have immediately followed melilite, so we tried modeling both possibilities. The chondrite-normalized REE abundances predicted for a perovskite crystallized from the resulting residual liquid are compared to those of a REE-rich perovskite from TS32 in Figure 8b. The model predicts slightly higher LREE abundances and much lower Yb and Lu abundances than are observed.

The measured TS32 fassaite REE patterns are quite unusual and cannot be matched by any fractional crystallization model. Note from Figure 7b that the LREE abundances in this fassaite are less than those of melilite. They are inconsistent with crystallization after any melilite with $D_{\text{LREE}} < 1$, (i.e., more magnesian than $\sim \dot{A}k_g$). Our calculations show that, if fassaite crystallized after spinel and melilite, but before perovskite, it would have REE abundances one to two orders of magnitude higher than are observed. If it followed perovskite and was the last phase to crystallize, it would have LREE contents much lower and HREE much higher than observed because of the strong preference of perovskite for LREE over HREE (Kennedy et al., 1994; Simon et al., 1994b). Even if just the right amount of perovskite crystallized so that fassaite began crystallizing with the observed La content (the “fas match La” trend in Fig. 8b), calculations show that the fassaite REE pattern would have a much higher HREE/LREE ratio than is observed. If TS32 were once molten, the perovskite in it could have crystallized from the melt, but we cannot account for the REE patterns of the fassaite in this inclusion by any fractional crystallization model.

4.2.3. TS68

For this inclusion, we used unpublished INAA and modal data. We modeled the inclusion by crystallizing 10% spinel, all of the melilite (78% of the inclusion), and then fassaite. The calculated pattern for fassaite is nearly identical to the measured one, as shown in Figure 8c. This good fit, the similarity of the chondrite-normalized REE patterns of TS68 fassaite to those of fassaite from type B1 inclusions (e.g., Simon et al., 1991), and the rounded, smooth shape of the inclusion all indicate that it crystallized from a liquid.

4.2.4. A37

Here we used the INAA data of Bischoff et al. (1987) and modal proportions from a backscattered electron photomosaic of the inclusion. This sample contains fassaite, perovskite, and rhönite, any one of which could have immediately followed melilite. Assuming fassaite is the first phase to crystallize after melilite (“fas before pv” in Fig. 8d), the measured composition of fassaite has lower LREE and higher Yb and Lu contents than expected. The results for perovskite, assuming that it follows melilite and precedes fassaite (“pv before fas”), are a fairly good fit, except for Yb, and this crystallization sequence leads to a better fit between calculated and observed LREE abundances in fassaite (“fas after pv”). As in TS32, however, prior crystallization of perovskite yields fassaite that is more HREE-enriched than is observed. We cannot model rhönite crystallization because no D s are available for this phase. We note, however, that it has chondrite-normalized HREE $>$ LREE (Fig. 7d). Perhaps rhönite crystallized immediately after perovskite, driving down the HREE/LREE ratio of the liquid from which fassaite subsequently crystallized.

4.2.5. Ef3

The bulk composition and modal mineralogy of this inclusion were determined by Sylvester et al. (1993). In the model we crystallized 20% spinel, and then 57% melilite to match the observed La content of fassaite. This is consistent with the observation that the inclusion contains $\sim 20\%$ fassaite (Sylvester et al., 1993). The results (Fig. 8e) show excellent agreement between the observed and calculated fassaite compositions, with the exceptions of Yb and Lu. The trace-element contents of fassaite in Ef3 and its occurrence in interstitial pockets between melilite (Fig. 2d) are consistent with formation of Ef3 from a melt, with crystallization of fassaite from the late, residual liquid.

4.2.6. AX4

For this inclusion we used the unpublished INAA data that were discussed by Yoneda et al. (1995) and modal proportions from a backscattered electron photomosaic of the inclusion. In this inclusion, as in TS12, melilite was followed by perovskite whose chondrite-normalized REE patterns range from very REE-rich with LREE $>$ HREE to flat patterns with lower absolute abundances (Fig. 7f). If perovskite dominates the crystallizing assemblage, the LREE-enriched pattern would be consistent with relatively early perovskite and the flat pattern consistent with late perovskite. Our calculations (Fig. 8f) show

that, except for Yb and Lu, the chondrite-normalized REE abundances and pattern of perovskite crystallized from the residual liquid in AX4 after crystallization of 92% of the inclusion to spinel + melilite are very similar to those of the relatively LREE-rich perovskite found in the inclusion. This inclusion has a spinel–perovskite core (Fig. 2e), which was most likely formed by the pushing inward of spinel and residual melt during solidification of the melilite. Although spinel is the liquidus phase in most type A and type B inclusion compositions (Paque and Stolper, 1984; Beckett, 1986), many CTAs and BIs have spinel-poor outer zones (~ 500 – ~ 1000 μm wide) and relatively spinel-rich inner zones, suggesting that spinel grains were commonly pushed toward inclusion interiors by advancing crystallization fronts. The perovskite in the core of AX4 probably represents the last liquid to crystallize. This is probably the case for AX30 as well, which also has a spinel-rich, perovskite-rich core and perovskite that texturally appears to have crystallized after melilite.

4.2.7. Summary

In summary, good agreement is observed between the calculated and observed LREE (Ce and Sm) abundances in at least one phase in all samples, and between calculated and observed Gd, Dy, and Ho contents in most samples. Perovskite tends to have higher Eu and, except for TS12, Yb and Lu contents than are predicted, however. Perhaps the values of $D^{\text{pv/liq}}$ used for these elements were too low, leading to underestimations of their abundances. The mismatch between the calculated and observed Lu contents of TS12 perovskite, with calculated $>$ observed, is different from that in other samples and may reflect a problem with either the RNAA analysis of the sample (Grossman et al., 1977) or the ion-probe analysis of the perovskite (Laughlin et al., 1986). We also cannot readily account for the mismatch between the observed and calculated REE patterns for fassaite in TS32. The observed patterns are quite unusual; they are unlike those seen in fassaite in the other CTAs or in type B inclusions (e.g., Simon et al., 1991), and are not consistent with the crystal/liquid D s determined for fassaite (Simon et al., 1991). It would be of interest to see whether the fassaite in 3898, another CTA with many features that are not consistent with crystallization from a melt (Podosek et al., 1991), has similar characteristics.

The general agreement seen above between observed chondrite-normalized REE patterns and those predicted by fractional crystallization models strongly suggests that the distribution of trace elements between phases in CTAs was largely determined by crystal–liquid partitioning. The degree of agreement, while not perfect, would be quite fortuitous if the phases were condensates whose REE contents were determined by crystal–vapor partitioning. Although gas–solid partition coefficients for the phases considered here are not known, one might expect that they would be volatility-related and differ from the crystal–liquid partition coefficients.

In addition to the distribution of trace elements, many petrographic and mineral-chemical features of CTAs are consistent with crystallization from liquids, including:

1. Rounded shapes and smooth rims of inclusions. These are also exhibited by type B inclusions and by chondrules, in

which they result from solidification of molten droplets. In contrast, fluffy type As do not have round shapes.

2. Melilite grains that are oriented at high angles to inclusion rims (e.g., Fig. 1a, 2b) and are zoned with Åk contents increasing inward from them (e.g., Fig. 3c). This is seen in type B1 inclusions and reflects nucleation upon and growth inward from a melt/vapor meniscus (e.g., MacPherson and Grossman, 1981).
3. Spinel-poor outer regions and relatively spinel-rich interiors. These are also commonly seen in type B1 inclusions and thought to reflect the pushing inward of spinel grains by growing melilite crystals.
4. Positively correlated V_2O_3 and Sc_2O_3 contents in fassaite. Both oxides are compatible in fassaite, decreasing from the cores to the rims of fassaite in type B inclusions (e.g., Simon et al., 1991). Such a trend would not necessarily be expected for condensates, because Sc is more refractory than V and these two elements can be fractionated from each other during condensation. For example, some ultrarefractory inclusions are exceedingly enriched in Sc but not in V (Davis, 1984; Simon et al., 1996).
5. Perovskite–spinel–fassaite symplectites. It is very unlikely that these features formed by gas–solid condensation, but they could have formed by crystallization of late, Ti-rich liquids (El Goresy et al., 1977; Beckett, 1986).
6. Occurrence of fassaite and perovskite in interstitial pockets between melilite grains, as shown in Figure 2d and f, in which the shapes of the Ti-rich phases have conformed to the shapes of the enclosing melilite grains. These textural relationships are consistent with the formation of these Ti-rich phases by crystallization of late-stage melt pockets, as is also suggested by the fractional crystallization models.

The unzoned melilite grains could have formed from either a liquid or a vapor. The coarse grain size and lack of zoning probably reflect growth during very slow cooling. The sawtooth zoning pattern of the melilite in TS12 (Fig. 3b) may reflect small temperature fluctuations during crystallization. Reversely zoned melilite can occur in once-molten, type B inclusions, but, in those cases, is attributed to the incoming of fassaite, which drives down the Mg/Al ratio of the residual liquid and of cocrystallizing melilite (MacPherson et al., 1984). This effect is unlikely to account for the reverse zoning in TS32, however. This inclusion contains very little fassaite, and the trace element-data are not consistent with the fassaite and the melilite being cogenetic. The irregular shape of the inclusion, the reverse zoning from core to rim of some melilite grains, the bimodal distribution of melilite compositions, and fassaite trace-element contents all suggest that much of TS32 may never have been molten. The Sc_2O_3 -, HREE-rich fassaite and the reversely zoned melilite in this inclusion may be relict grains.

4.3. Precursor Phases

The samples considered here do not represent pristine condensates, but they probably formed by crystallization of partial melts of condensate assemblages. Sylvester et al. (1993) considered the bulk compositions of a large suite of coarse-grained refractory inclusions from Allende and members of the reduced

subgroup of CV3 chondrites. For Allende, “prealteration” bulk compositions were calculated. These investigators noted that all of the type A (FTA and CTA) inclusions in their suite have superchondritic CaO/Al₂O₃ ratios and that many of their bulk compositions plot on or near the trajectory of compositions of condensates from a solar gas that had lost ~20% of its Al₂O₃, perhaps due to corundum condensation. Some type As have subchondritic TiO₂/Al₂O₃ ratios as well, possibly reflecting prior removal of hibonite from the gas (Sylvester et al., 1993). Beckett and Stolper (1994) also concluded that corundum was not likely to have been among the precursor phases of type As, suggesting a phase assemblage of melilite + spinel + hibonite + perovskite. The precursors of type B inclusions, on the other hand, probably continued to react with the nebular gas to lower temperatures, at least until fassaite condensed, resulting in higher average SiO₂ and MgO contents of type B inclusions than type As (Sylvester et al., 1993).

Although FTAs and CTAs have identical average CaO and TiO₂ contents, most CTAs have higher SiO₂ and lower Al₂O₃ contents than FTAs (Sylvester et al., 1993). Except for two cases noted by Sylvester et al. (1993), CTAs therefore cannot simply be isochemical melted analogs of the present suite of FTAs. They may, however, be melts of former, relatively less refractory FTAs. As shown by Sylvester et al. (1993), bulk compositions of CTAs plot along the SiO₂-rich, Al₂O₃-poor end of a linear trend defined by CTA and FTA bulk compositions on a plot of SiO₂ vs. Al₂O₃. The precursor assemblages of CTAs may have had lower melting points, and therefore melted more readily, than the relatively Al₂O₃-rich FTAs.

4.4. Crystallization Histories

Teshima and Wasserburg (1985) studied three CTAs, one of which they described as completely recrystallized and consisting of homogeneous minerals. Greshake et al. (1998) studied three CTAs, including A37 with the electron microprobe and transmission electron microscope (TEM), and found those samples to be dominated by unzoned mineral grains with many 120° triple junctions. They also found, with the TEM, high dislocation densities in melilite but none in fassaite which, along with untwinned spinel, suggests that shock events took place at temperatures ≥1000°C. On the basis of their work, Greshake et al. (1998) concluded that CTAs were shocked while plastic and were later recrystallized at temperatures <1000°C. In the present study we observed recrystallized melilite in AX30 and Ef3 optically, whereas laths and blocky crystals dominated the other samples viewed in thin section. Although some inclusions were recrystallized and individual crystals somewhat homogenized, grain-to-grain variations were not erased; the CTAs we studied typically exhibited ranges of ~30 mol% Åk (Fig. 4), and the trace element distributions reflected crystal/liquid partitioning, suggesting, in agreement with Greshake et al. (1998), that any reheating event was mild.

5. CONCLUSIONS

We have studied eight compact type A refractory inclusions in order to document, for the first time in one study, the petrographic, mineral-chemical, and trace-element characteristics of a representative suite of this major type of refractory inclusion. Compact type A inclusions have long been assumed

by many to have crystallized from melts, but until now there was very little evidence to support this assumption. Although, by definition, these inclusions are strongly dominated by melilite, they may contain, in addition to melilite and spinel, perovskite, perovskite + Ti-rich fassaite, or perovskite + fassaite + rhönite. These inclusions have enough features in common that a plausible sequence of events can be proposed for their formation. First, assemblages of condensate precursors, most likely melilite + spinel + perovskite ± hibonite, melted. Melting was not complete, because, as in type Bs, melilite textures are not consistent with crystallization from total melts (Stolper and Paque, 1986). Features of CTAs that suggest that they crystallized from melts include rounded inclusion shapes; radially oriented melilite laths at inclusion rims, with Åk contents increasing inward from the inclusion rims; spinel-poor outer regions and spinel-rich interiors; and the distribution of trace elements among phases. We were, in many cases, able to reproduce quantitatively with fractional crystallization models, the REE contents of perovskite and fassaite in CTAs we studied. In contrast, virtually no features of CTAs are consistent with origins as either volatilization residues or as gas–solid condensates. Many CTAs were shocked, as indicated by the presence of shock lamellae and high dislocation densities (Greshake et al., 1998). Finally, recrystallization of some inclusions occurred during a mild reheating event, which led to formation of 120° triple junctions but did not cause intergranular redistribution of major, minor, or trace elements. One CTA we studied, TS32, showed several features (irregular shape, reversely zoned melilite, bimodal distribution of melilite compositions, fassaite REE contents) that could not be readily explained by crystallization from a melt. It may be dominated by relict grains that underwent only a very small degree of melting.

Acknowledgments—The authors acknowledge the Field Museum of Natural History for the loan of Axtell samples, C. Palenik for digital image collection, and J. R. Beckett for helpful discussions. Reviews provided by A. Greshake and an anonymous reviewer led to improvements in the text. This work was supported by the National Aeronautics and Space Administration through Grants NAGW-3340 and NAG5-4476 (L. G.), NAGW-3384 and NAG5-4298 (A.M.D.), and NAGW-3345 and NAG5-3986 (to R. N. Clayton), and funding is gratefully acknowledged.

REFERENCES

- Beckett J. R. (1986) The origin of calcium-, aluminum-rich inclusions from carbonaceous chondrites: An experimental study. Ph.D. dissertation, Univ. Chicago.
- Beckett J. R., Spivack A. J., Hutcheon I. D., Wasserburg G. J., and Stolper E. M. (1990) Crystal chemical effects on the partitioning of trace elements between mineral and melt: An experimental study of melilite with applications to refractory inclusions from carbonaceous chondrites. *Geochim. Cosmochim. Acta* **54**, 1755–1774.
- Beckett J. R. and Stolper E. (1994) The stability of hibonite, melilite and other aluminous phases in silicate melts: Implications for the origin of hibonite-bearing inclusions from carbonaceous chondrites. *Meteoritics* **29**, 41–65.
- Bischoff A. and Palme H. (1987) Composition and mineralogy of refractory-metal-rich assemblages from a Ca, Al-rich inclusion in the Allende meteorite. *Geochim. Cosmochim. Acta* **51**, 2733–2748.
- Bischoff A., Palme H., and Spettel B. (1987) A37-A coarse-grained, volatile element-poor Ca-, Al-rich inclusion with huge Fremdlinge. *Lunar Planet. Sci.* **XVIII**, 81–82 (abstr.).
- Casanova I. and Grossman L. (1993) Distribution of vanadium and melting of opaque assemblages in Efremovka CAIs. *Lunar Planet. Sci.* **XXIV**, 257–258 (abstr.).

- Davis A. M. (1984) A scandalously refractory inclusion in Ornans. *Meteoritics* **19**, 214 (abstr.).
- Davis A. M., Simon S. B., and Grossman L. (1990) Trace element distributions in Allende compact type A inclusions. *Meteoritics* **25**, 356 (abstr.).
- Davis A. M., Simon S. B., and Grossman L. (1992) Melilite composition trends during crystallization of Allende Type B1 refractory inclusion melts. *Lunar Planet. Sci.* **XXIII**, 281–282 (abstr.).
- Davis A. M., Richter F. M., Simon S. B., and Grossman L. (1996) The effect of cooling rate on melilite/liquid partition coefficients for Y and REE in Type B CAI melts. *Lunar Planet. Sci.* **XXVII**, 291–292 (abstr.).
- El Goresy A., Nagel K., and Ramdohr P. (1977) Type A Ca-, Al-rich inclusions in Allende meteorite: Origin of the perovskite-fassaite symplectite around rhönite and chemistry and assemblages of the refractory metals (Mo, W) and platinum metals (Ru, Os, Ir, Re, Rh, Pt). *Meteoritics* **12**, 216 (abstr.).
- El Goresy A., Nagel K., and Ramdohr P. (1978) Fremdlinge and their noble relatives. *Proc. 9th Lunar Planet. Sci. Conf.*, 1279–1303.
- Fahey A., Zinner E., Crozaz G., and Kornacki A. S. (1987) Microdistributions of Mg isotopes and REE abundances in a Type A calcium-aluminum-rich inclusion from Efremovka. *Geochim. Cosmochim. Acta* **51**, 3215–3229.
- Floss C., El Goresy A., Zinner E., Kransel G., Rammensee W., and Palme H. (1996) Elemental and isotopic fractionations produced through evaporation of the Allende CV chondrite: Implications for the origin of HAL-type hibonite inclusions. *Geochim. Cosmochim. Acta* **60**, 1975–1997.
- Fuchs L. H. (1971) Occurrence of wollastonite, rhönite, and andradite in the Allende meteorite. *Am. Min.* **56**, 2053–2067.
- Fuchs L. H. (1978) The mineralogy of a rhönite-bearing calcium aluminum rich inclusion in the Allende meteorite. *Meteoritics* **13**, 73–88.
- Greshake A., Bischoff A., and Putnis A. (1998) Transmission electron microscope study of compact Type A calcium-aluminum-rich inclusions from CV3 chondrites: Clues to their origin. *Meteoritics Planet. Sci.* **33**, 75–87.
- Grossman L. (1975) Petrography and mineral chemistry of Ca-rich inclusions in the Allende meteorite. *Geochim. Cosmochim. Acta* **39**, 433–454.
- Grossman L. (1980) Refractory inclusions in the Allende meteorite. *Ann. Rev. Earth Planet. Sci.* **8**, 559–608.
- Grossman L. and Ganapathy R. (1976) Trace elements in the Allende meteorite—I. Coarse-grained, Ca-rich inclusions. *Geochim. Cosmochim. Acta* **40**, 331–344.
- Grossman L., Ganapathy R., and Davis A. M. (1977) Trace elements in the Allende meteorite—III. Coarse-grained inclusions revisited. *Geochim. Cosmochim. Acta* **41**, 1647–1664.
- Haggerty S. E. (1976) Titanium cosmochimetry and rhönite decomposition in Allende. *Meteoritics* **11**, 294 (abstr.).
- Kennedy A. K., Lofgren G. E., and Wasserburg G. J. (1994) Trace-element partition coefficients for perovskite and hibonite in meteorite compositions. *Chem. Geol.* **117**, 379–390.
- Kuehner S. M., Laughlin J. R., Grossman L., Johnson M. L., and Burnett D. S. (1989) Determination of trace element mineral/liquid partition coefficients in melilite and diopside by ion and electron microprobe techniques. *Geochim. Cosmochim. Acta* **53**, 3115–3130.
- Kurat G. (1970) Zur Genese der Ca-Al-reichen Einschlüsse im Chondriten von Lancé. *Earth Planet. Sci. Lett.* **9**, 225–231.
- Kurat G. (1975) Der kohlige Chondrit Lancé: Eine petrologische Analyse der komplexen Genese eines Chondriten. *Tschermaks Min. Petr. Mitt.* **22**, 38–78.
- Laughlin J. R., Hinton R. W., Grossman L., and Davis A. M. (1986) Ion microprobe study of rim and core perovskite in an Allende inclusion. *Meteoritics* **21**, 430–431.
- MacPherson G. J. and Davis A. M. (1993) A petrologic and ion microprobe study of a Vigarano Type B refractory inclusion: Evolution by multiple stages of alteration and melting. *Geochim. Cosmochim. Acta* **57**, 231–243.
- MacPherson G. J. and Davis A. M. (1994) Refractory inclusions in the prototypical CM chondrite, Mighei. *Geochim. Cosmochim. Acta* **58**, 5599–5625.
- MacPherson G. J. and Grossman L. (1979) Melted and non-melted coarse-grained Ca-, Al-rich inclusions in Allende. *Meteoritics* **14**, 479–480.
- MacPherson G. J. and Grossman L. (1981) A once-molten, coarse-grained, Ca-rich inclusion in Allende. *Earth Planet. Sci. Lett.* **52**, 16–24.
- MacPherson G. J. and Grossman L. (1984) “Fluffy” Type A Ca-, Al-rich inclusions in the Allende meteorite. *Geochim. Cosmochim. Acta* **48**, 29–46.
- MacPherson G. J., Paque J. M., Stolper E., and Grossman L. (1984) The origin and significance of reverse zoning in melilite from Allende Type B inclusions. *J. Geol.* **92**, 289–305.
- Martin P. M. and Mason B. (1974) Major and trace elements in the Allende meteorite. *Nature* **249**, 333–334.
- Mason B. and Taylor S. R. (1982) Inclusions in the Allende meteorite. *Smithsonian Contrib. Earth Sci.* **25**, 1–30.
- McSween H. Y. (1977) Petrographic variations among carbonaceous chondrites of the Vigarano type. *Geochim. Cosmochim. Acta* **41**, 1777–1790.
- Molini-Velsko C. (1983) Isotopic composition of silicon in meteorites. Ph.D. dissertation, Univ. Chicago.
- Paque J. M. and Stolper E. (1984) Crystallization experiments on a range of Ca–Al rich inclusion compositions. *Lunar Planet. Sci.* **XV**, 631–632 (abstr.).
- Podosek F. A., Zinner E., MacPherson G. J., Lundberg L. L., Brannon J. C., and Fahey A. J. (1991) Correlated study of initial $^{87}\text{Sr}/^{86}\text{Sr}$ and Al–Mg isotopic systematics and petrologic properties in a suite of refractory inclusions from the Allende meteorite. *Geochim. Cosmochim. Acta* **55**, 1083–1110.
- Pouchou J. L. and Pichoir F. (1984) A new model for quantitative x-ray microanalysis. Part I: Application to the analysis of homogeneous samples. *Rech. Aerosp.* **3**, 13–38.
- Simon S. B., Grossman L., and Davis A. M. (1991) Fassaite composition trends during crystallization of Allende Type B refractory inclusion melts. *Geochim. Cosmochim. Acta* **55**, 2635–2655.
- Simon S. B., Grossman L., and Wacker J. F. (1994a) Unusual refractory inclusions from a CV3 chondrite found near Axtell, Texas. *Lunar Planet. Sci.* **XXV**, 1275–1276 (abstr.).
- Simon S. B., Kuehner S. M., Davis A. M., Grossman L., Johnson M. L., and Burnett D. S. (1994b) Experimental studies of trace element partitioning in Ca, Al-rich compositions: Anorthite and perovskite. *Geochim. Cosmochim. Acta* **58**, 1507–1523.
- Simon S. B., Davis A. M., and Grossman L. (1995) Crystallization of compact Type A refractory inclusions: Implications for crystal zoning and trace element distribution. *Lunar Planet. Sci.* **XXVI**, 1303–1304 (abstr.).
- Simon S. B., Davis A. M., and Grossman L. (1996) A unique ultrarefractory inclusion from the Murchison meteorite. *Meteoritics Planet. Sci.* **31**, 106–115.
- Simon S. B., Davis A. M., and Grossman L. (1998) Formation of an unusual compact Type A refractory inclusion from Allende. *Meteoritics Planet. Sci.* **33**, 115–126.
- Stolper E. and Paque J. M. (1986) Crystallization sequences of Ca–Al-rich inclusions from Allende: The effects of cooling rate and maximum temperature. *Geochim. Cosmochim. Acta* **50**, 1785–1806.
- Sylvester P. J., Simon S. B., and Grossman L. (1992) Chemical compositions of Fremdlinge from a Type A Allende inclusion. *Lunar Planet. Sci.* **XXIII**, 1397–1398 (abstr.).
- Sylvester P. J., Simon S. B., and Grossman L. (1993) Refractory inclusions from the Leoville, Efremovka, and Vigarano C3V chondrites: Major element differences between Types A and B, and extraordinary refractory siderophile element compositions. *Geochim. Cosmochim. Acta* **57**, 3763–3784.
- Teshima J. and Wasserburg G. J. (1985) Textures, metamorphism and origin of Type A CAI's. *Lunar Planet. Sci.* **XVI**, 855–856 (abstr.).
- Wark D. A. and Lovering J. F. (1977) Marker events in the early evolution of the solar system: Evidence from rims on Ca–Al-rich inclusions in carbonaceous chondrites. *Proc. 8th Lunar. Sci. Conf.*, 95–112.
- Wark D. A. and Lovering J. F. (1982) Evolution of Ca–Al-rich bodies in the earliest solar system: Growth by incorporation. *Geochim. Cosmochim. Acta* **46**, 2595–2607.
- Yoneda S., Simon S. B., and Grossman L. (1995) Chemical compositions of refractory inclusions in Axtell, a CV3 chondrite of the oxidized subgroup. *Lunar Planet. Sci.* **XXVI**, 1541–1542 (abstr.).